

Key Points:

- Degraded impact craters called hollows at both the InSight and Spirit landing sites appear similar in morphology from orbital and surface images
- The clasts within *Homestead* hollow are similar in size and shape to those within *Laguna* hollow, with most resolvable clasts ranging from 3–7 mm in length
- The hollow similarities at two different landing sites suggest recent environmental conditions that degrade and infill craters are comparable and pervasive

Correspondence to:

C. M. Weitz,
weitz@psi.edu

Citation:


Weitz, C. M., Grant, J. A., Golombek, M. P., Warner, N. H., Hauber, E., Ansan, V., et al. (2020). Comparison of InSight *Homestead* hollow to hollows at the Spirit landing site. *Journal of Geophysical Research: Planets*, 125, e2020JE006435. <https://doi.org/10.1029/2020JE006435>

Received 2 MAR 2020

Accepted 1 JUN 2020

Accepted article online 10 JUN 2020

Comparison of InSight *Homestead* Hollow to Hollows at the Spirit Landing Site

Catherine M. Weitz¹ , John A. Grant² , Matthew P. Golombek³ , Nicholas H. Warner⁴ , Ernst Hauber⁵ , Veronique Ansan⁶, Sharon A. Wilson², Constantinos Charalambous⁷ , Nathan Williams³ , Fred Calef³, W. Thomas Pike⁷ , Heather Lethcoe-Wilson³, Justin Maki⁴ , Alyssa DeMott⁴, and Megan Kopp⁴

¹Planetary Science Institute, Tucson, AZ, USA, ²Center for Earth and Planetary Studies, National Air and Space Museum, Smithsonian Institution, Washington, DC, USA, ³Jet Propulsion Laboratory, California Institute of Technology, Pasadena, CA, USA, ⁴Department of Geological Sciences, SUNY Geneseo, Geneseo, NY, USA, ⁵Institute of Planetary Research, German Aerospace Center (DLR), Cologne, Germany, ⁶Laboratory of Planetary and Geodynamics, University of Nantes, Nantes, France, ⁷Department of Electrical and Electronic Engineering, Imperial College, London, UK

Abstract The InSight spacecraft landed within an ~27-m diameter highly degraded impact crater, informally called *Homestead* hollow, that was disturbed during landing by pulsed retrorockets that blew out dust and scoured loose sand around the landing site. In order to provide insight into what the surface of *Homestead* hollow originally looked like before landing and to further characterize hollow physical properties, we examined images of similar hollows taken by the Spirit rover at the Gusev landing site. Hollows at both sites are characterized by a quasi-circular appearance with little or no crater rim still visible and a bright interior with fewer and smaller rock sizes relative to the surrounding plains. Resolvable clast lengths (>2 mm) measured in *Laguna* hollow at the Spirit site and *Homestead* hollow are comparable with most clasts between 3 and 7 mm in length. Measurements of clast shapes show that those in *Laguna* hollow are slightly more elongate relative to those in *Homestead* hollow, although this may be an artifact of the differing viewing geometry and (or) a thicker dust mantle obscuring the full shape of clasts at *Laguna* hollow. The soils at both hollows show evidence for cohesion and a duricrust, with a trench dug at *Laguna* hollow and pits exposed at *Homestead* hollow exhibiting steep slopes, overhanging layers, and clods of soils. The similarities in morphology and physical properties of hollows at two different landing sites suggest recent environmental conditions that degrade and infill impact craters are comparable and pervasive for equatorial volcanic plains on Mars.

1. Introduction

The Interior Exploration using Seismic Investigations, Geodesy and Heat Transport (InSight) spacecraft landed successfully on Mars in western Elysium Planitia on 26 November 2018 (Figure 1). Images taken by the Instrument Deployment Camera (IDC) (Maki et al., 2018) across the landing site reveal a shallow (~0.3 m) depression with a relatively low rock abundance (1–2% for rocks >10-cm diameter) compared to the terrain on the rim and beyond (Golombek et al., 2020; Grant et al., 2020). The interpretation of the landing site based upon available surface and orbital images is that InSight landed on the western side of a quasi-circular soil-filled ~27-m diameter depression with a rocky rim inferred to be a former impact crater, hereafter referred to as a “hollow” (Golombek et al., 2020; Grant et al., 2020; Warner et al., 2020). Hollows are part of a morphologic continuum that is caused by progressive crater rim destruction from mass wasting, impacts, and eolian abrasion, combined with infilling of the crater by preferential preservation/accumulation of fines within a topographic depression (Golombek, Crumpler et al., 2006; Grant, Arvidson et al., 2006; Grant et al., 2020; Sweeney et al., 2018; Warner et al., 2020). The age of the InSight landing region is Early Hesperian based on the cumulative SFD of craters >5 km in diameter (Tanaka et al., 2014). More recent crater counts confirm the Early Hesperian age for craters with diameters greater than 2 km, but for smaller craters (200-m to 1-km diameter), the age is Early Amazonian (Golombek et al., 2018; Warner et al., 2017) likely due to volcanic resurfacing. This resurfacing completely buried small craters while embaying/preserving ghost-like examples of larger craters.

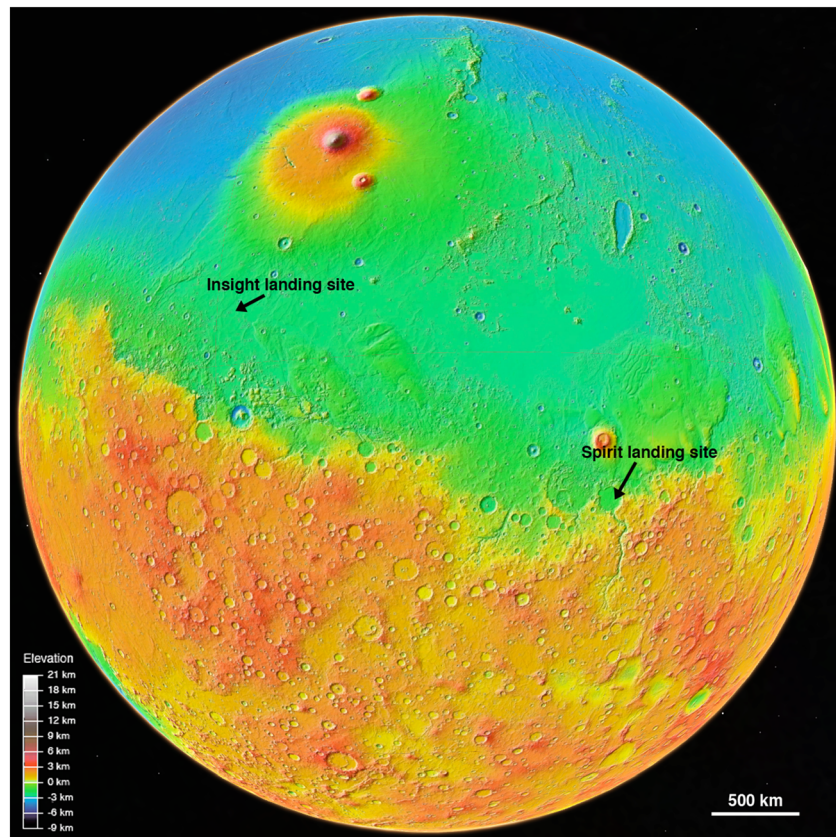


Figure 1. Mars Orbiter Laser Altimeter (MOLA) (Smith et al., 2001) global shaded relief with elevations shown by color. The locations of the InSight landing site in western Elysium Planitia (4.50°N , 135.62°E) and the Spirit landing site in Gusev crater (14.57°S , 175.48°E) are noted. Both landing sites occur in the northern lowlands where there has been volcanic resurfacing. North is toward the top.

During the InSight landing into the informally named *Homestead* hollow, the spacecraft used thrusters to slow the descent. Camera images taken of the surface around the lander show linear scouring emanating from the lander as a result of the retrorockets removing fine dust and displacing sands around the landing site, which is supported by orbital camera images that show a blast zone surrounding the lander (Figure 2) (Williams et al., 2019). Consequently, the landing site represents a disturbed rather than a pristine surface. In order to provide insight into what the surface of *Homestead* hollow originally looked like before landing, we examined images of several hollows that were explored by the Mars Exploration Rover (MER) Spirit rover during its exploration of the Gusev crater lava plains.

Spirit landed in the $\sim 160\text{-km}$ diameter Gusev crater (Figure 1) on 3 January 2004 (Squyres et al., 2004). The floor of Gusev crater was selected as the landing site both because it fit the engineering criteria for a safe landing site (Golombek et al., 2003; Grant et al., 2004) and because it was postulated that the interior of Gusev crater had been filled in with fluvial and lacustrine sediments from Ma'adim Vallis (Cabrol et al., 2003), making it a compelling science target for exploration. Upon landing, however, Spirit discovered that the floor of Gusev is covered by basaltic lava, and no evidence of fluvial or lacustrine sediments was viewed nearby the landing site. The Gusev plains where Spirit landed have been dated to Hesperian (Greeley et al., 2005), with some units showing modification and redistribution during the Amazonian (Golombek, Crumpler, et al., 2006; Milam et al., 2003; Wilson et al., 2020).

Images taken by cameras on the Spirit rover at the landing site and after driving to the northeast showed the terrain is marked by numerous hollows. Like at *Homestead* hollow, the Gusev hollows are interpreted as degraded impact craters due to their roughly circular planform (Golombek, Crumpler, et al., 2006; Grant, Arvidson, et al., 2006). Consequently, Spirit images taken of undisturbed hollows at Gusev crater can be used to infer more information about what the undisturbed surface of *Homestead* hollow may have looked like

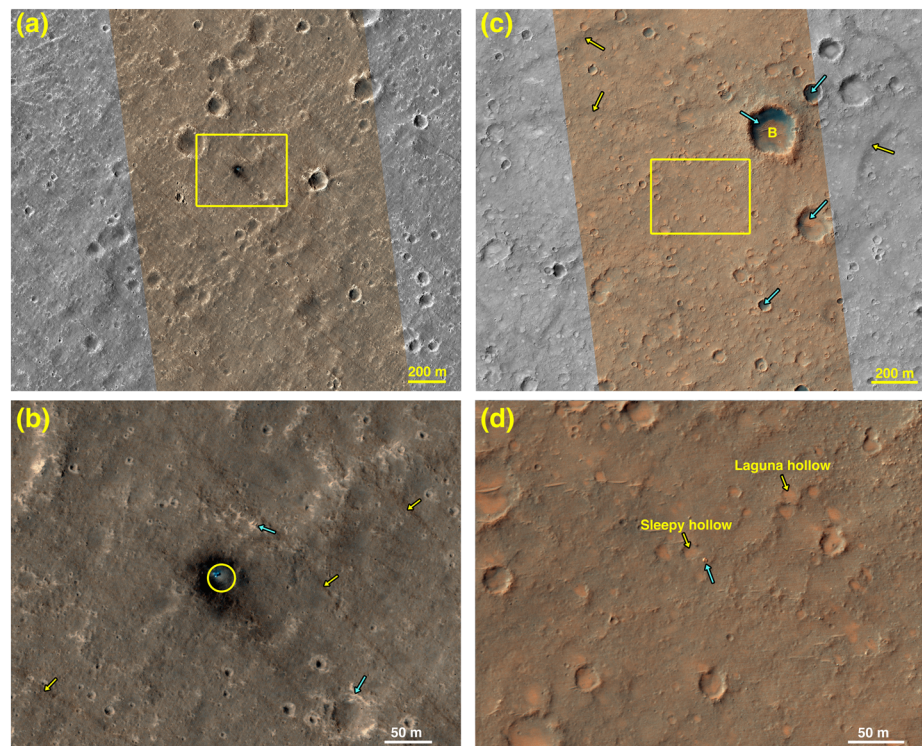


Figure 2. (a) Portion of HiRISE image ESP_061684_1845_MRGB showing the InSight lander and blast zone in Elysium Planitia. Yellow rectangle shows the location of the blowup in panel (b). Illumination is from the left, and north is to the top. (b) The InSight lander and solar panels appear blue, whereas the blast zone produced by the thruster rockets is black. Yellow circle marks the approximate *Homestead* hollow rim. Yellow arrows identify darker streaks that could have formed by dust devils or wind scouring in the NW to SE direction. Blue arrows identify bright eolian bedforms within impact craters. (c) Portion of HiRISE image ESP_02070_1655_MRGB taken of the Spirit landing site. The yellow rectangle identifies the location of the blowup shown in panel (d). Blue arrows point to dark eolian sands and bright eolian bedforms within impact craters. Yellow arrows note dark dust devil tracks. The letter “B” identifies Bonneville crater. Illumination is from the left, and north is to the top. (d) The blue arrow shows the lander where the Spirit rover began its journey across Gusev crater. *Sleepy hollow* and *Laguna hollow* are also noted.

prior to landing. Additionally, Spirit drove into an ~18-m diameter hollow informally called *Laguna* and used its wheels to dig an ~6–7 cm deep trench into the hollow soils (Arvidson et al., 2004). The images of the subsurface in *Laguna* hollow can be compared to images of the subsurface at *Homestead* hollow exposed during landing and deployment of the geophysics instruments to further understand Martian soils and their physical properties.

Because there is no bedrock exposed at the InSight landing site, the rocks in *Homestead* hollow reveal important clues regarding the geology of the area, especially the bedrock in the subsurface and the transport and erosional history affecting the region. In this study, we explore the morphology of the hollows at both landing sites using orbital and surface images and then measure the rock sizes and shapes at both *Homestead* and *Laguna* hollows to compare these characteristics at two different landing sites. Our results have implications for the development and modification of hollows and soils on Mars.

2. Data Sets

2.1. HiRISE and CTX

Orbital data collected by the Mars Reconnaissance Orbiter (MRO) Context Camera (CTX) (Malin et al., 2007) and High Resolution Imaging Science Experiment (HiRISE) (McEwen et al., 2007) provide ~6 m and ~26 cm/pixel scales of the InSight and Spirit landing sites, respectively. Data from HiRISE are collected by the red channels (550 to 850 nm) to produce a monochrome image, whereas blue-green (400 to 600 nm) and near-infrared (800–1,000 nm) channels allow a narrower color image within the red image. HiRISE

images were acquired before and after landing to show the undisturbed and disturbed surface of *Homestead* hollow. The HiRISE images taken after landing show a dark spot that extends ~20 m away from the lander to the north (Figures 2a and 2b). The dark spot resulted from removal of dust by thruster jets that were used during descent and landing. The Spirit landing did not produce this same broad dark spot because the landing system used airbags (Crisp et al., 2003) that resulted in smaller bounce marks on the surface.

2.2. InSight

The InSight IDC is attached to the forearm of a four degree of freedom arm used to deploy the instruments onto the surface, which also includes a scoop at the end that can interact with surface materials (Trebilcock et al., 2018). The IDC is a flight spare of the Mars Science Laboratory (MSL) Navcam camera, which in turn is a copy of the MER Navcam that is on the Spirit rover (Maki et al., 2003). The only difference between the IDC and MER/MSL Navcams is that the gray-scale detector has been replaced by a Bayer color filter array (CFA) version of the same detector in order to obtain color images. The IDC has a medium field of view (FOV) with a resulting instantaneous FOV (IFOV) of 0.82 mrad/pixel, identical to the MER/MSL Navcams (Maki et al., 2018). Spatial resolution in an IDC image depends on the position of the camera relative to the ground, with the closest ground position at a range of 0.65 m corresponding to a spatial resolution of ~0.5 mm/pixel. Images we utilized from the IDC include stereo coverage at two resolutions (0.5 and 2 mm/pixel) of the instrument deployment workspace (~4 m × ~3 m) to select the locations to place the geophysical instruments to the southeast in front of the lander and three complete stereo panoramas (morning, afternoon, and evening) acquired from a height of ~1.5 m above the surface. The Heat Flow and Physical Properties Package (HP3) includes a mole designed to penetrate up to 5 m beneath the surface (Spohn et al., 2018). Unfortunately, the mole has not yet been able to penetrate down beneath ~35 cm for unknown reasons, but the ~5 cm wide hole exposed by the mole provides useful information about the subsurface. Similarly, the excavation pits produced by the thrusters during landing also reveal information about the subsurface (Ansan et al., 2019; Golombek et al., 2020).

2.3. Spirit

The Spirit rover has six wheels that are 26 cm in diameter and 16 cm wide with 6 mm deep cleats (Geissler et al., 2010). Each of the wheels exerts a force of ~108 N under Martian gravity (Richter et al., 2006; Sullivan et al., 2007) and can provide information about the soil strength based upon the rover track imprints. The rover also has a high-resolution camera called Pancam (Bell, 2004; Bell et al., 2003). Pancam is a multispectral, stereoscopic, panoramic imaging system consisting of two digital cameras mounted on a mast 1.5 m above the Martian surface. Each camera has an eight position filter wheel to allow surface mineralogic studies in the 400- to 1,100-nm wavelength region. Pancam has a 0.27-mrad/pixel instantaneous field of view, corresponding to ~1 mm/pixel at a range of 3 m from the rover (Bell, 2004; Bell et al., 2003). In addition to Pancam, the Spirit rover also has stereo broadband monochrome navigation cameras (Navcam) (Maki et al., 2003). The Navcam angular resolution at the center of the field of view is 0.82 mrad/pixel, corresponding to ~3 mm/pixel at a range of 3 m from the rover. In this study, we utilized the Pancam and Navcam images taken of the hollows and rover track imprints on the hollow soils to further understand the morphology of several hollows at Gusev crater and the clast physical properties within these hollows.

3. Orbital Views of InSight and Spirit Landing Sites

3.1. InSight Landing Site Region

Orbital images taken by the CTX and HiRISE cameras provide a regional view of the terrain around each landing site. Prelanding mapping and assessment of the InSight landing site region suggested a volcanic plain with a surface composed of cohesionless sand size particles, some rocks, and thermally thin coatings of dust (Golombek et al., 2017). The InSight landing site region in HiRISE images appears smooth with impact craters having a subdued and degraded appearance (Figure 2a), except for the smaller recent secondary craters from Corinto (Golombek et al., 2017). For the ejecta/rim morphology, smaller, 10-m-scale craters lack rocks in their ejecta blankets and generally lack rocky rims at the HiRISE resolution. This is due to the presence of a 3- to 5-m-thick loosely consolidated regolith layer (Sweeney et al., 2018; Warner et al., 2017). Larger, 100-m-scale craters are much more rocky, indicating excavation of a rocky unit. These larger craters also hold steeper slopes relative to smaller craters, which is consistent with different target materials (Sweeney et al., 2018; Warner et al., 2017). Soils within the degraded craters and hollows appear similar in

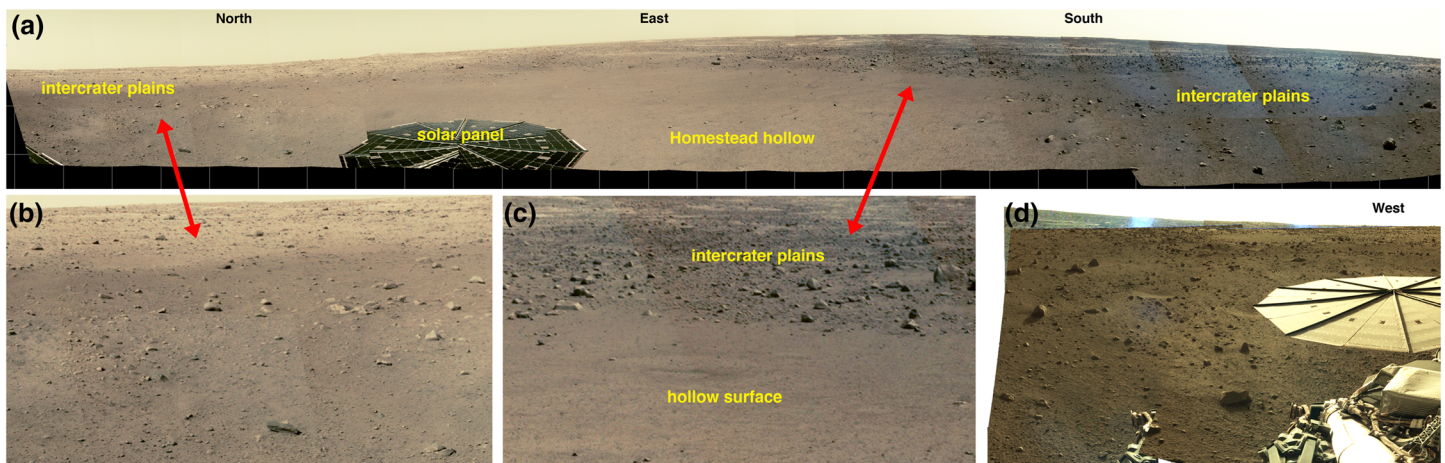


Figure 3. (a) Instrument Deployment Camera (IDC) partial mosaic ($\sim 300^\circ$ azimuth around lander) of the InSight landing site with compass directions noted. The solar panel is 2.2 m in size for reference. (b) In this blowup, the boundary of the hollow is difficult to identify because the interior of the hollow appears similar in morphology and rock abundance to the exterior intercrater plains. (c) Blowup showing the dichotomy between the smoother hollow surface with few large rocks compared to the rougher and rockier intercrater plains. (d) IDC images of the western side of the landing site. The western edge of the hollow appears rockier compared to elsewhere within the hollow. The solar panel is 2.2 m in size for reference.

color and brightness to the intercrater plains. Some of the craters have darker interior patches that could be either dark eolian sands or younger exposed bedrock along the crater rims. Bright eolian bedforms are sometimes found within or adjacent to older craters (Figure 2b) and very commonly observed in ejecta, against the rims, and within all relatively fresh craters.

3.2. Spirit Landing Site Region

HiRISE images of the hollows and craters around the Spirit landing site show better defined rims and larger topographic relief than at InSight (Figure 2). Craters at InSight are not rocky at all scales and therefore may be different from those at Gusev because of differences in the regolith properties/surface processes at the two sites. Large meter-size boulders are resolvable in the HiRISE images for both sites and most likely represent ejecta fragments from younger craters. In particular, Bonneville crater (210-m diameter) located to the northeast of the Spirit landing site (Figure 2c) has a blocky ejecta field that extends out to *Laguna* hollow (about one crater diameter). Dark eolian sands and bright bedforms are observed inside many craters (Figure 2c). The Spirit landing site and traverses were within a darker zone with numerous dust devil tracks at the center of Gusev crater relative to the rest of the crater floor as seen in CTX images. Craters outside this dark zone appear to have the same brightness as the intercrater plains, similar to what is observed at the InSight landing site. Thus, some of the differences between the Spirit and InSight landing sites as seen from orbital data may reflect the higher abundance of dark and mobile eolian sand at the Spirit site. In particular, soils within the hollows at the Spirit site appear brighter relative to the soils outside (Figure 2d), which likely reflects the contrast in appearance between the dust collecting inside these depressions relative to dark eolian sand found in the intercrater plains.

4. Morphology of the InSight and Spirit Hollows From Surface Images

4.1. Homestead Hollow

Using the IDC mosaics taken of the area around the lander (Figure 3), we can infer some information about the morphology of *Homestead* hollow. Although the hollow lacks an appreciable elevated rim, there are portions of the hollow that have an abrupt and significant increase in cobble to boulder size rocks along the approximate rim and on the intercrater plains as compared to the relatively smooth interior (Grant et al., 2020). A classification scheme of crater preservation at the InSight landing region identifies *Homestead* hollow as an example of the most degraded, Class 8 craters (Warner et al., 2020). The InSight landing region appears modified by impact, eolian, and mass wasting processes with the surface composed of >3 m thick impact-fragmented regolith overlying basalt flows (Golombek et al., 2020; Grant et al., 2020; Warner et al., 2020).

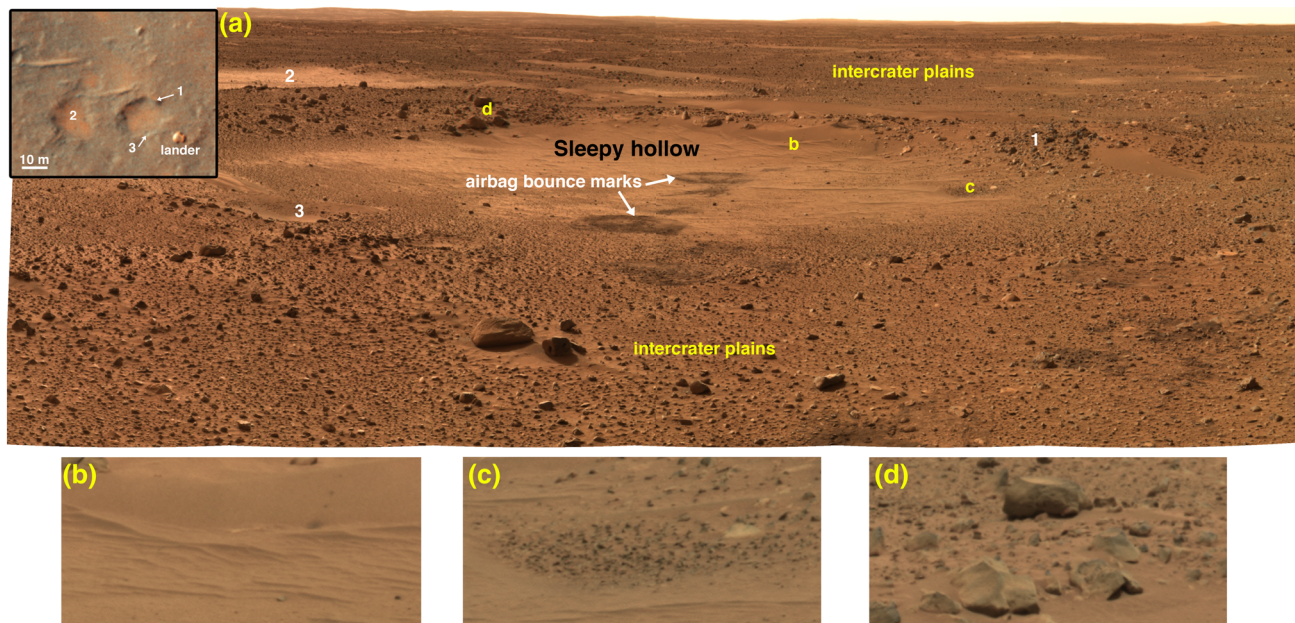


Figure 4. (a) Pancam mosaic (Sol009A_P2354_L456atc) showing the view of *Sleepy hollow* (~17 m diameter) and nearby terrain as seen from the Spirit landing site (view is looking to the northwest). Numbers identify the same features shown on the HiRISE (ESP_028070_1655_RGB) blowup inset (upper left), where 1 = northeastern rim, 2 = hollow to the west, and 3 = small (~1 m diameter) crater on the southern rim of *Sleepy hollow*. Letters correspond to the locations of blowups in panels (b)–(d). The airbag bounce marks produced during the landing are also noted. Note that the HiRISE image was acquired several years after the Spirit landing so the airbag bounce marks have faded and are no longer visible from orbit. (b) Blowup of eolian sands and ripples observed on the floor of *Sleepy hollow*. (c) Cluster of cobbles exposed on the floor where the eolian mantle is thinner. (d) Large boulders seen along the northwestern rim of *Sleepy hollow*.

The observed float rocks in *Homestead hollow* are likely ejecta that were delivered to this location by impacts (Charalambous et al., 2019; Grant et al., 2020). Views to the south from the lander and within approximately 15- to 20-m distance show a surface dominated by sand to pebble-size materials. The southeastern side of the hollow has a similar distribution of rocks relative to the adjacent plains (Figure 3b), making the crater margin harder to discern here than elsewhere (e.g., Figure 3c). The western side of the hollow (Figure 3d) dubbed “Rocky Field” (Golombek et al., 2020) has the highest abundance of rocks, and the rocks are larger relative to the rocks elsewhere within the hollow. Grant et al. (2020) interpret the greater number of rocks at Rocky Field to represent ejecta rocks, likely from a crater located to the northwest. There are no eolian ripples or accumulation of sand piles within the hollow, but these features may have been destroyed by the retro-rockets during landing.

4.2. Spirit Hollows

We analyzed Pancam and Navcam images taken by Spirit that cover several of the hollows around the landing site. The informally named *Sleepy hollow* is an ~17-m diameter hollow that was seen from the Spirit landing platform (Figure 2d). The darker airbag bounce marks are visible within the hollow (Figure 4a), indicating that a thin veneer of bright dust covers the surface and the floor of the hollow appears brighter relative to the intercrater plains. Bright eolian ripples and thick accumulations of sand/dust are common along the hollow floor (Figure 4b). A small patch of densely clustered cobbles is observed in the northern portion of the floor (Figure 4c), and additional cobble clusters are found along the western and southern edges of the floor where the eolian mantle is likely thinner.

The northern edge of *Sleepy hollow* rim has a well-defined topographic profile, as seen in both Pancam and HiRISE images. Large boulders are abundant along this same rim (Figure 4d). In contrast, the southern rim cannot be easily identified in topography, although the rock abundance increases abruptly from the hollow floor to where the rim is presumed to lie. A small ~1-m diameter impact crater is seen along the southern rim of *Sleepy hollow* in both the HiRISE and Pancam images (Figure 4a, location 3). This small crater does not expose larger rocks in the subsurface, and its floor is covered by smooth bright dust.

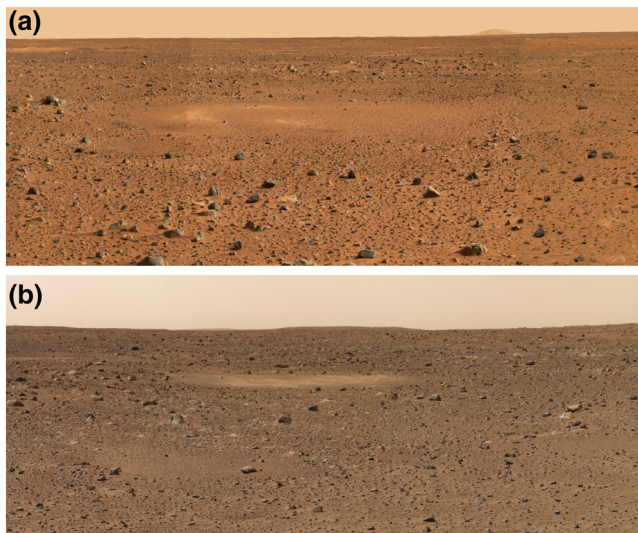


Figure 5. (a) Pancam mosaic of an ~10-m diameter unnamed hollow a few meters south of the Spirit landing site. There is minimal topography associated with the rim, and the floor is clearly smoother with fewer large rocks relative to the surrounding intercrater plains. Image Sol029A_P2381_L247atc. (b) Pancam mosaic of an ~10-m diameter hollow observed on Sol 40 with a bright interior and eolian ripples visible. The bright surface and paucity of larger rocks relative to the intercrater plains makes the hollow easy to identify even though there is no obvious rim. Image Sol40A_P2780_L456atc.

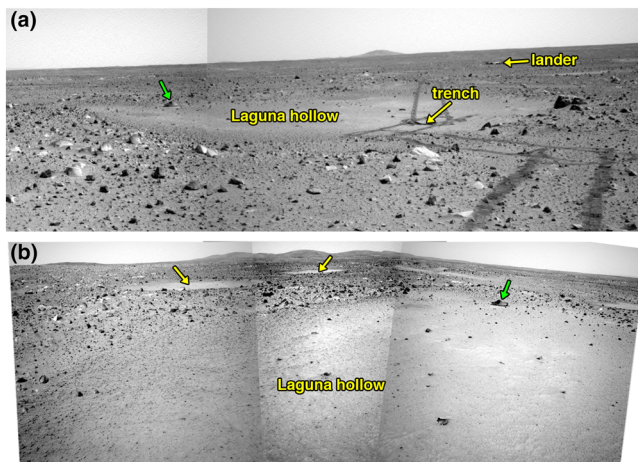


Figure 6. (a) Navcam mosaic (images 2N130812149EFF1000P1901L0M1 and 2N130812099EFF1000P1901R0M1 on Sol 50) of *Laguna* hollow (~18-m diameter) taken as Spirit drove away after trenching inside the hollow. The lander is also visible in this view looking to the southwest. Left-side and right-side rover tracks are 1.2 m apart for scale. The green arrow identifies a large boulder which is also noted by a green arrow in panel (b) that shows the eastern side of *Laguna* hollow taken while Spirit was inside the hollow. Note the increase in cobble-size clasts moving from the hollow interior (lower right) to the rim (left). Yellow arrows point to smaller hollows located to the east. The Columbia Hills are seen in the distance. Navcam images 2N130365005EFF0900P1817R0M1, 2N130366302EFF0900P1835R0M1, and 2N130366339EFF0900P1835R0M1 taken on Sol 45.

A smaller unnamed hollow is visible a few meters to the south of the Spirit landing site (Figure 5a). The rim is difficult to identify in the Pancam data due to the lack of relief associated with the impact feature. The floor of the unnamed hollow appears brighter and has fewer of the larger rocks relative to the intercrater plains surrounding it. In the HiRISE images, this unnamed hollow has a slightly brighter interior than its surroundings and a quasi-circular outline. We estimate the diameter of the hollow to be ~10 m from the HiRISE images. Similarly, another small hollow imaged near the landing site on Sol 40 does not have an obvious rim, although its bright floor is clearly visible in the Pancam mosaic relative to the intercrater plains surrounding it (Figure 5b). Eolian ripples are visible inside the hollow, and there are very few cobbles or larger rocks within the hollow.

On Sol 42, Spirit drove inside an ~18-m diameter hollow informally called *Laguna*. Navcam images taken of *Laguna* hollow show a smooth, bright floor and a very degraded rim (Figure 6). The rim has minimal relief, best seen along the northwestern side where there is a large boulder (Figure 6a). A close-up view of the eastern side of the hollow (Figure 6b) shows the paucity of larger rocks along the floor relative to the surrounding rim and intercrater plains. There are numerous cobbles on the hollow floor that increase in abundance moving away from the interior and toward the rim. Eolian ripples of variable length and height occur closer to the hollow interior. Additional hollows with smooth bright floors are visible to the east of *Laguna* (Figure 6b).

5. Clast Sizes Within Hollows

5.1. Homestead Hollow

After landing, images taken by the IDC were used to characterize *Homestead* hollow and determine the physical properties of the work volume around the lander in order to select a safe and benign area to deploy the seismometer SEIS (Lognonné et al., 2019, 2020) and heat flow probe HP3 (Spohn et al., 2018). The instruments had to be placed on a smooth, relatively flat, load-bearing surface with their feet placed firmly on the ground and with no rocks or relief greater than 3 cm (Golombek et al., 2017). We utilized the highest resolution IDC mosaic acquired from orthorectified images taken at 0.5–1 mm per pixel spatial scale to measure the sizes of all clasts, here defined as loose granule to cobble-sized rock fragments on the surface, larger than 1.5–2 mm (gravel size) within the instrument footprints on the surface where it was assumed they could be deployed.

We measured the maximum length of a total of 1,965 particles in the SEIS instrument footprint and 1,288 particles in the HP3 footprint (Figure 7a) that appeared to be >70% in area above the surface (i.e., <30% buried). Particles were measured manually using the National Institute of Health public software package ImageJ (Schneider et al., 2012) based upon our visual inspection of each clast to determine the major axis. A line was then drawn across this major axis to calculate the length. We only measured particles that were 3 pixels or larger such that the smallest particles we could measure at the highest available image mosaic resolution (0.5 mm/pixel) was 1.5 mm across. The median length for particles at the SEIS deployment site is 3.7 mm with a range of 2–23 mm (Figure 7b), and for the HP3 footprint, the median length is 3.6 mm

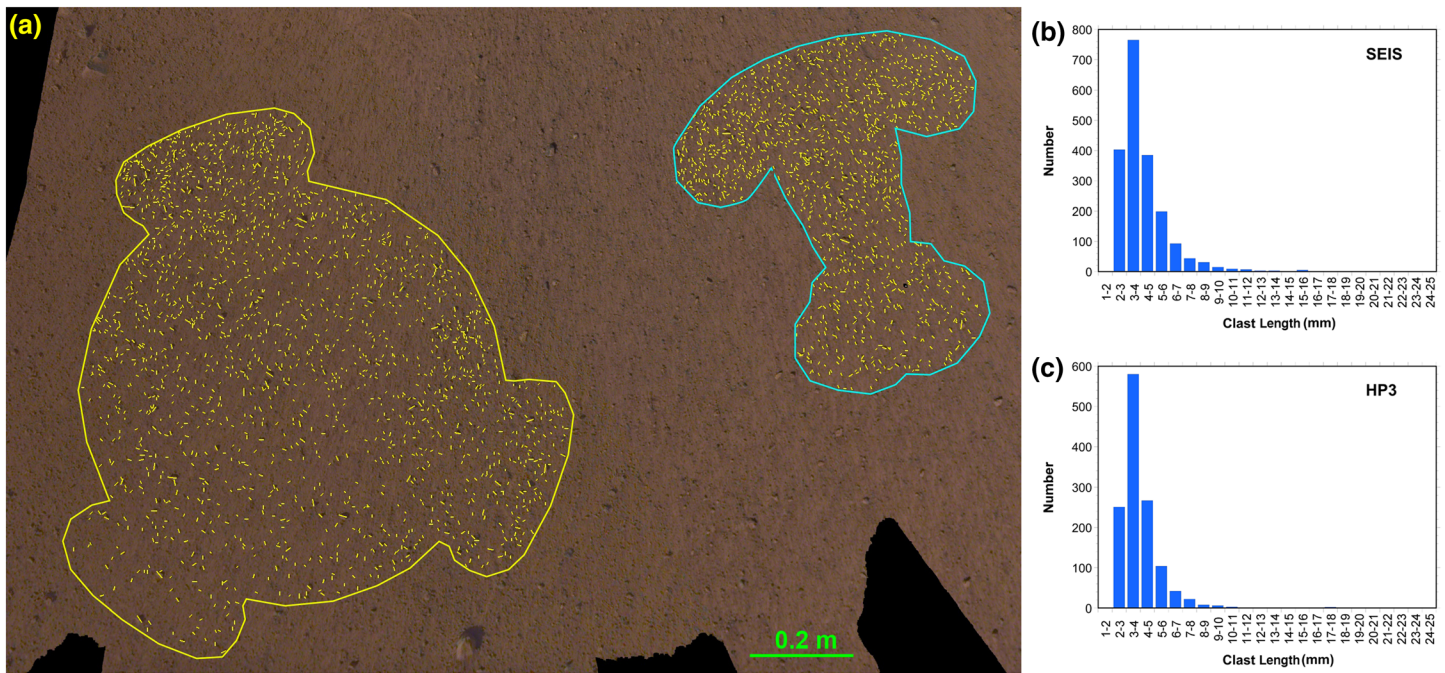


Figure 7. (a) Portion of IDC mosaic of the work volume prior to instrument deployment. The outlines of the SEIS (left, yellow) and HP3 (right, blue) instruments with placement error uncertainties are noted. Yellow lines within each instrument footprint show individual grains >1.5 mm in size that were measured for their maximum length. Plots of clasts sizes within the SEIS footprint (b) and the HP3 footprint (c) show most clasts fall between 3 and 4 mm. Illumination from lower left.

over a range of 2–17 mm (Figure 7c). The dominant resolvable particles size at both instrument deployment locations is 3–4 mm. It should be noted that much of the surface appears to be dominated by the finer size particles below 1.5 mm in size based upon disturbance of the soils by deployment of the SEIS and HP3 instruments, sculpting of loose sand by the retrorockets during landing to create linear tails behind larger particles, as well as divots in the soil made by the movement of loose pebbles during landing (Golombek et al., 2020; Weitz, 2019).

Once the HP3 and SEIS instruments were deployed on the surface shortly after landing, we measured clasts within the entire terrain south of the landing site that includes the instrument footprints where we initially made clast size measurements. For this slightly larger area (5.339 m^2), we digitized a total of 8,252 clasts in a GIS environment using the highest resolution (0.5–1 mm/pixel) IDC mosaic as a base map. The length of each clast was determined with the ArcGIS tool Minimum Bounding Geometry. All clasts were measured down to a minimum length of 6 pixels, corresponding to 3 mm for the smallest clast length. Measured sizes range from 3–58 mm in length with a median value of 5.3 mm and the majority of clasts between 4 and 7 mm in size (Table 1). Thus, all clasts we measured are granule to pebble size, falling between 2 and 64 mm as defined by Wentworth (1922). If we include clasts within the larger but lower resolution IDC mosaic taken at 1–2 mm/pixel scale, then there are several larger cobbles up to 120 mm in length.

5.2. Laguna and Homestead Size Comparison

In order to compare an equal number of clast sizes from *Homestead* and *Laguna* hollow, we measured the major axis (length) of 800 clasts at both hollows. At *Laguna* hollow, we used a Pancam mosaic taken on Sol 46 of the rover tracks across the hollow surface (Figure 8a). The resolution of the Pancam images varies with range to the surface. Because we do not know at what distance the *Laguna* hollow floor mosaic was acquired from the rover, we cannot determine the precise resolution to use for this mosaic at varying range. However, the rover tracks are visible in the image, and we know that each rover wheel is 16 cm wide, which enables determining the Pancam pixel scale using the rover wheel tracks in the

Table 1
Physical Properties of Clasts at Homestead and Laguna Hollows

Site	Homestead	Laguna 1	Laguna 2
Best image scale (mm/pixel)	0.5	0.7	0.4
Length range (mm)	3–58	3–50	2–32
Median length (mm)	5.3	6.4	4.3
Circularity range	0.67–0.98	0.56–0.96	0.56–0.94
Median circularity	0.90	0.84	0.83
Aspect ratio range	1.0–2.6	1.0–3.6	1.1–2.9
Median aspect ratio	1.38	1.63	1.67

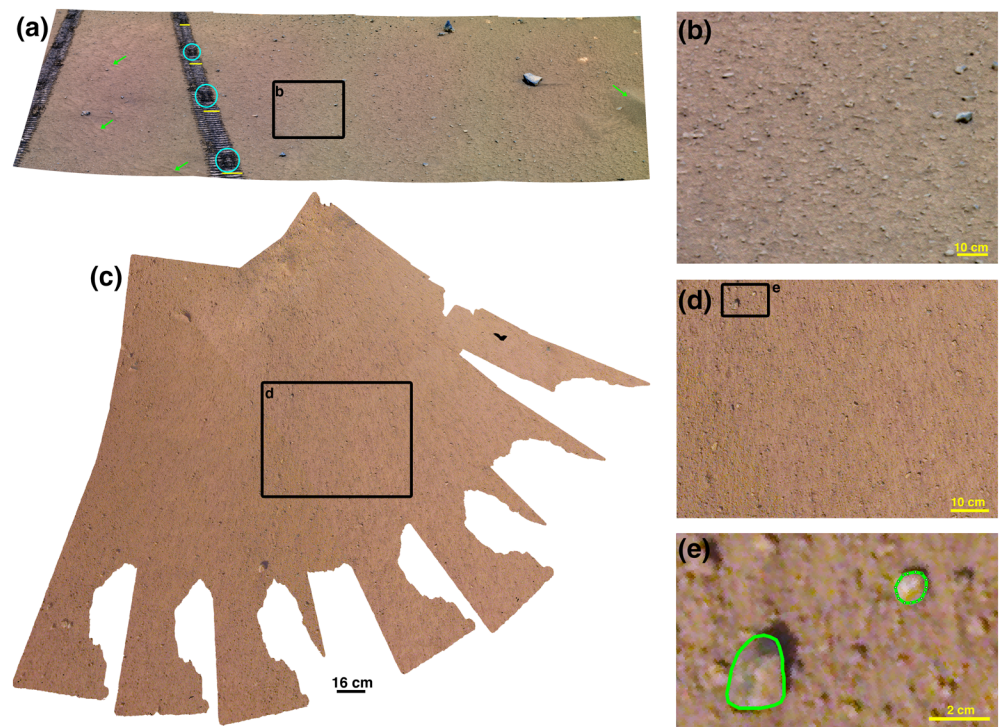


Figure 8. (a) Pancam mosaic (Sol046A_P2417_L457atc) of the *Laguna* hollow floor at location *Laguna* 1. The blue circles are drawn around rectangular imprints in one of the wheel tracks that are spaced apart by one wheel circumference. Yellow lines drawn on the wheel tracks represent the 16-cm width of each wheel. Green arrows identify eolian ripples in the left of the image, and the green arrow to the far right shows a larger eolian ripple. Black rectangle is the location of the blowup in panel (b), which shows numerous pebbles on the surface and partially buried within the soil. (c) IDC mosaic at 0.5-mm/pixel spatial resolution of the *Homestead* hollow floor. Black rectangle is the location of the blowup in panel (d), which shows pebbles on a finer grained smooth surface. Note the lineations aligned from top to bottom that are scour and wind shadows created when the retrorockets blew away dust and fine sands. Black rectangle identifies the location of the blowup shown in panel (e). (e) Example of outlines (green ovals) made using the ImageJ software that were manually drawn around clasts to calculate shapes. The upper right clast also shows the 15 vertex points (white squares embedded within green line) that we made to define each clast shape (see text for description).

image as a scale. In reality, the wheel tracks are likely greater than 16 cm wide because the leading, middle, and trailing wheels do not follow the exact same path during driving and thus cover a broader width than one single wheel. Luckily, the topmost wheel track is distinguishable from the lower wheel tracks in the Pancam mosaic due to a rectangular imprint that is made with each wheel rotation (Figure 8a). Using this knowledge about the rectangular wheel imprint, we were able to measure the width of one wheel track and used this as the 16-cm scale to calculate a Pancam resolution of 0.7 mm/pixel for the foreground of the image where we measured the clast sizes. The smallest clast we could resolve at this resolution, assuming a minimum of 3 pixels in length, is 2 mm. However, the hollow soil is dusty, and for all clasts below 3 mm in size, it was difficult to identify the clast edges to measure a precise length, which is why in actuality the smallest clasts we measured from this mosaic were 3 mm. For this Location 1 in *Laguna* hollow, we calculate a median length of 6.4 mm for grains >3 mm in size with a range from 3–50 mm (Table 1; Figure 9).

The 800 clasts we measured at *Homestead* hollow were taken from a smaller subset of the 0.5-mm/pixel resolution IDC mosaic (Figure 8d), but the sizes are consistent with those measured across the entire IDC mosaic, albeit with a slightly smaller median length (4 mm) relative to the median length measured for the larger workspace (5.3 mm). As seen in the clast size histogram (Figure 9), the interior of *Homestead* hollow is characterized by smaller clasts relative to *Laguna* 1, which could be a result of the higher resolution of the camera images or the lack of a dust mantle at *Homestead* compared to *Laguna* hollow, making it easier to see and measure the smaller (3- to 4-mm size) clasts.

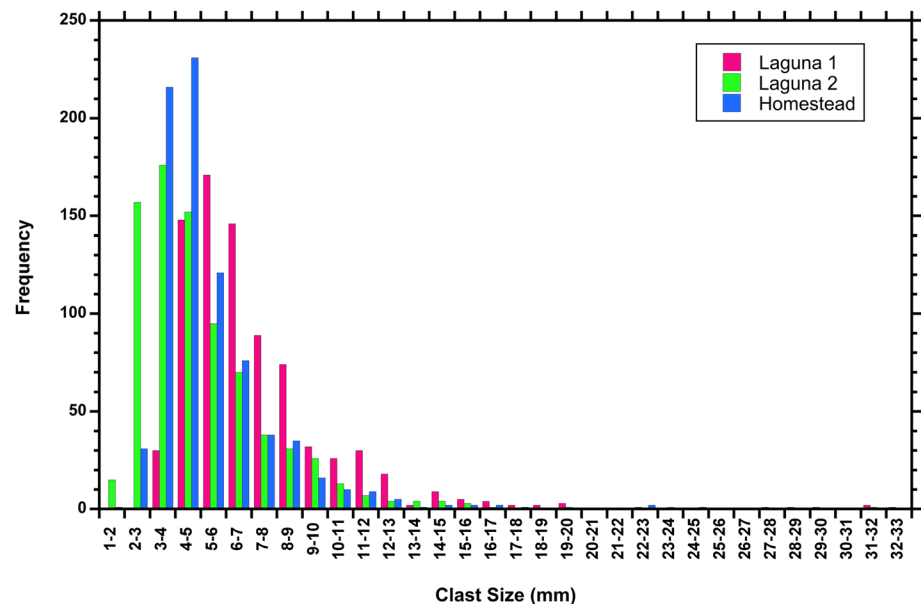


Figure 9. Plot showing the sizes for 800 clasts measured at *Homestead* hollow and two locations in *Laguna* hollow.

In order to evaluate the effect of resolution and particle dust cover on grain size measurements, we also measured the size of 800 clasts in a Pancam mosaic taken of the trench dug into the *Laguna* hollow soils (Figure 10a). This workspace mosaic was taken at a closer range from the Spirit rover with a resolution assumed to be 0.4 mm/pixel (Yingst et al., 2008) that is more comparable to the 0.5 mm/pixel *Homestead* mosaic. The median length measured for this *Laguna* 2 location is 4 mm (Table 1), exactly that measured for the *Homestead* subset. Interestingly, there is a larger population of 2- to 3-mm size clasts at this *Laguna* 2 location than what we measured for *Homestead* (Figure 9). These smaller clasts could be due to the slightly better resolution for the *Laguna* 2 mosaic relative to the *Homestead* IDC mosaic. Nevertheless, the sizes are very similar at both hollows.

6. Clast Shapes Within Hollows

6.1. *Homestead* Hollow

Particle shapes were measured for 142 clasts at *Homestead* that were situated on/above the surface (i.e., not buried by >30%) in the larger IDC 2-mm/pixel mosaic. We used the same imaging software program ImageJ, but to obtain a shape, we drew an outline around each clast. We selected clasts larger than 2 cm in length to ensure that a sufficient number of vertex points (>10) could be used to define the shape of each clast (Figure 8e). Circularity ($4\pi\text{Area}/\text{Perimeter}^2$) and aspect ratio (major axis length/minor axis length) were calculated by the software after each clast shape was outlined. We measured a median circularity of 0.9 and a median aspect ratio of 1.4 for the clasts at *Homestead* hollow (Table 1). Figure 11a shows a plot of the major axis versus the minor axis with almost all clasts having minor to moderate elongation, consistent with fracturing and fragmenting of basalts by impacts (Charalambous et al., 2019; Craddock & Golombek, 2016). It should be noted that our measurements only reflect the 2-D shape of the clasts due to the viewing geometry of the lander images. Ideally, the shape of each clast should be measured using three axes, as is done for rocks on Earth, to provide a more accurate measure of rock shape and for comparison to terrestrial samples (Craddock & Golombek, 2016), but this is not possible for the Martian clasts.

We also plotted the aspect ratio (also referred to as elongation and 2-D sphericity; Folk, 1974; Garvin et al., 1981) for these same clasts and compared these calculated values to a visual Krumbein and Sloss (1951) chart of grains as a function of increasing roundness (a measure of corner sharpness) and sphericity (how closely a clast profile resembles a sphere) (Figures 11b and 11c). The roundness is defined as the ratio of the average radius of curvature of the corners of a particle to the radius of the maximum inscribed circle (Wadell, 1932), but it can also be estimated visually using standard charts like the Powers scale

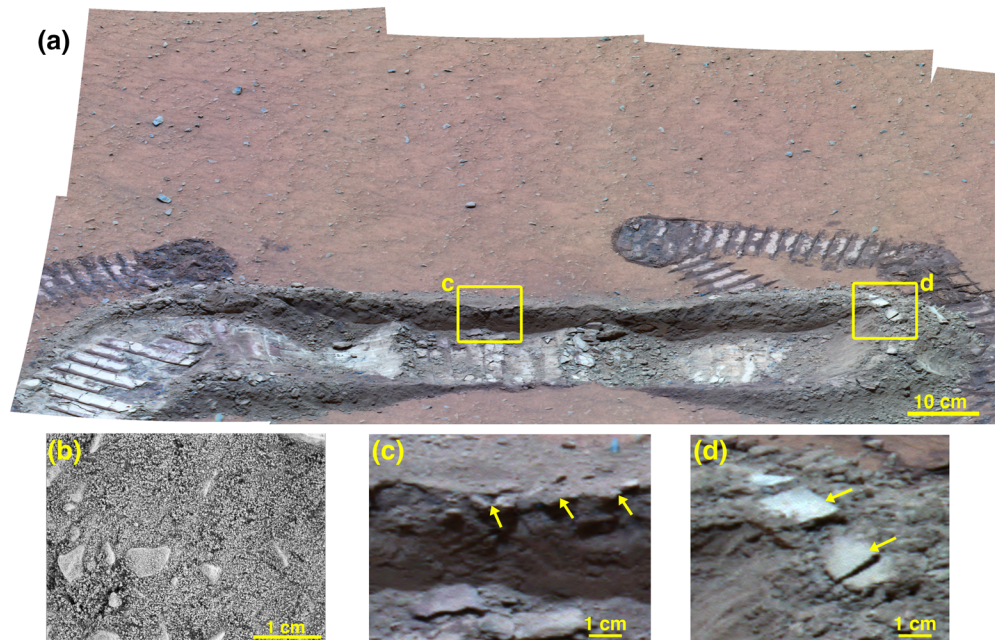


Figure 10. (a) Pancam mosaic Sol047A_P2418_L257F showing the trench dug into the *Laguna* hollow soil by the Spirit rover at location *Laguna* 2. Yellow rectangles identify the locations of the blowups in panels (c) and (d). A thin layer of bright, reddish air fall dust mantles undisturbed surfaces. (b) Microscopic Imager mosaic of images 2M130463097EFF0900P2953M2M1 and 2M130463749EFF0900P2953M2M1 taken on Sol 46 of the undisturbed surface of *Laguna* hollow. (c) Vertical exposure of the 6–7 cm deep trench wall showing fine-grained soil containing a few embedded pebbles. Yellow arrows identify an overhanging ledge near the top of the trench that indicates cohesion in the soil. (d) Clods of soil (yellow arrows) that were produced at the bottom of the trench by wheel compaction but later pushed outside the trench and laid down on top of a pile of displaced soil. Because the clods are still intact after this displacement, they must have cohesion.

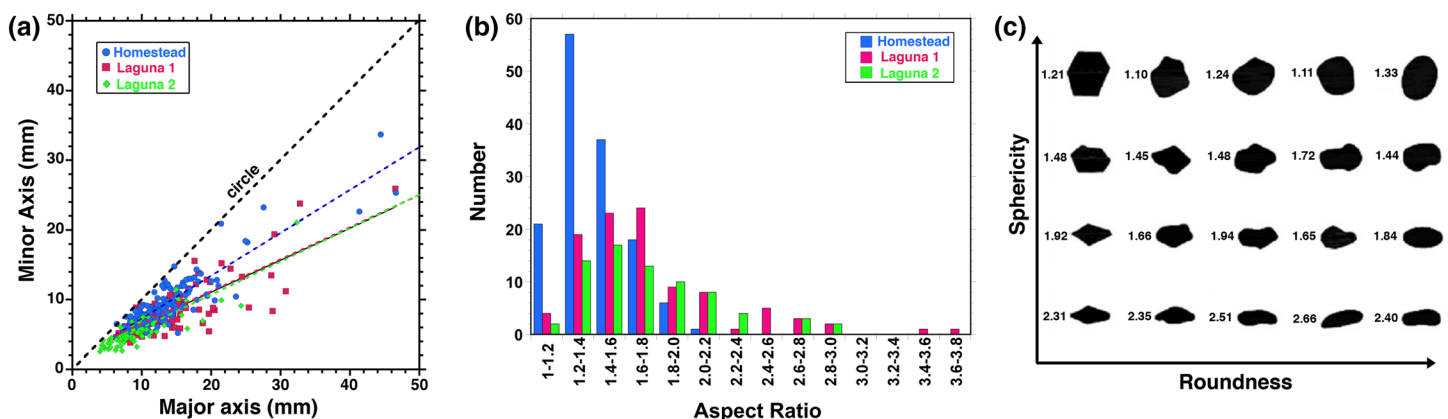


Figure 11. (a) Plot of the major and minor axis for clasts at *Homestead* and *Laguna* hollows. A perfect circle would plot along the black dashed line. Both hollows have elongated clasts, with those at *Laguna* hollow (red squares and green diamonds) more elongated relative to *Homestead* hollow clasts (blue circles). Dashed colored lines represent the best linear fit for clasts at each location. (b) Histogram of the aspect ratio for clasts measured at each location. At *Homestead*, 142 clasts were measured and the median aspect ratio is 1.38. For *Laguna* 1, 100 clasts were measured with a median aspect ratio of 1.63, and at *Laguna* 2, we measured 73 clasts with a median aspect ratio of 1.66. (c) Visual chart adapted from Krumbein and Sloss (1951) of particles with increasing roundness along the x axis and increasing sphericity along the y axis. Numbers next to each particle are the calculated aspect ratio. As roundness increases, the particles get smoother but their aspect ratios remain similar. As particles increase in sphericity, the particles appear more circular and their aspect ratios approaches the value of 1.0.

(Powers, 1953). Similarly, the sphericity is an approximation of how much the grain resembles a perfect sphere, and it too can be estimated visually using standard charts, which is different than the calculation of circularity determined by the ImageJ software. Because these methods to define roundness and sphericity are qualitative and subjective, caution is warranted. The grains that have an aspect ratio around 1.4 that we calculated as the median from ImageJ lie toward the upper right in the Krumbein-Sloss chart (Figure 11c), with the grains appearing slightly elongated as was also shown by the plot in Figure 11a.

Grain roundness/angularity are a function of transport history/degree of weathering and mineral hardness. The process of grain rounding becomes less efficient as grain size decreases, which means the shapes we measured for larger clasts at both sites could have been inherited from their sources rather than due to transport processes. When compared to the Powers scale, we visually assess most of the clasts at *Homestead* hollow range from subangular to subrounded, which is similar to measurements for the Spirit and average MSL Curiosity rover sites but more rounded than the clast populations at the Viking and Mars Pathfinder sites (Yingst et al., 2007, 2008, 2013). It should be noted that the camera resolution for Spirit and the Curiosity rovers is higher and thus smaller clasts can be assessed for morphology than was possible for the Viking and Pathfinder landed missions. Additionally, the size fraction for Viking and Pathfinder populations is larger in general, which skews the roundness toward more angular shapes.

6.2. Laguna Hollow

We also measured clast shapes across the entire Pancam mosaics of *Laguna 1* and *Laguna 2*. Because we are only using the ratio of the clast maximum and minimum axis to obtain the elongation, the changing pixel scale resolution across the large *Laguna 1* mosaic with distance from the rover does not affect this result. The plot of major versus minor axis for 100 clasts measured at *Laguna 1* and 73 clasts at *Laguna 2* is shown in Figure 11a. Our results show that clasts at *Laguna* hollow are more elongate relative to those at *Homestead* hollow. Additionally, the median circularity for clasts at both *Laguna 1* and *Laguna 2* is 0.8, which is less circular than the 0.9 value measured for clasts at *Homestead* hollow. The calculated aspect ratios also display a higher degree of elongation in the *Laguna* clasts (1.6–1.7), which is evident in the visual chart that shows aspect ratios with these values lie toward the middle of the chart in Figure 11c. The higher degree of elongation at *Laguna* relative to *Homestead* could be a real phenomenon or the result of the thicker dust mantle at *Laguna* that prevented us from seeing the entire shape of clasts that were partially buried within the dust. Because the dust was blown away from *Homestead* hollow during landing, we were able to view more of the clast shapes in this hollow. Additionally, the IDC images were acquired looking straight down on the surface, whereas the Pancam images of the *Laguna* hollow floor were taken at an angle that also hindered our ability to see the full shape of the clasts. Consequently, we believe the clast shapes measured at *Homestead* are more reliable than those at *Laguna* hollow.

Although there are a few, mostly larger (>5 cm) clasts that are vesicular and angular in appearance, most of the clasts at *Laguna 1* and *2* appear subangular to subrounded with no vesicles, similar to what is observed at *Homestead* hollow. Images taken by the Spirit Microscopic Imager on Sol 46 of the *Laguna 2* surface (Figure 10b) show a higher resolution view (31 $\mu\text{m}/\text{pixel}$; Herkenhoff et al., 2006) of the smaller clasts, including possible dust aggregates and coarser sand grains. At this resolution, the mm-size clasts lack vesicles and appear elongate in appearance. The roundness of the clasts appears less than that in the lower resolution Pancam mosaic because more corners and edges are now visible along the surface of each clast. The subangular to subrounded appearance of many of the clasts at both sites may have formed during the fracturing and fragmenting of the basalts that sourced these clasts (Craddock & Golombek, 2016) and (or) be the result of weathering, either from physical (e.g., eolian abrasion) or chemical (e.g., atmospheric water vapor) processes after the clasts were emplaced within the hollow. Some of the rounded appearance of clasts could simply reflect the resolution limits of the camera images we used to estimate roundness for these small pebble-size clasts.

7. Cohesion of the Soils

7.1. Homestead Hollow Soils

Images taken of the hollows at the InSight and Spirit sites show evidence for cohesion in the upper surface soils beneath the layer of unconsolidated sands and dust aggregates at both locations. Golombek et al. (2020) interpret the near-surface stratigraphy of the InSight landing site to have a microns-thick surficial cover of

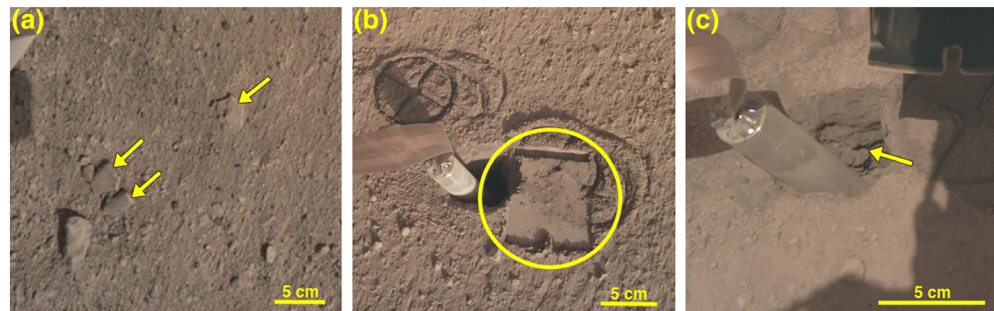


Figure 12. (a) Examples of possible soil clods (yellow arrows) observed adjacent to the InSight lander. Image D001L0012_597601745EDR_F0101_0060M2. Illumination from lower right. (b) Smooth and flat imprint (yellow circle) produced in the soils by the scoop as it pressed down on the surface next to the HP3 mole pit. The circular cross imprints of the underside of the HP3 footpad are also visible in the upper left. Image D000M0240_617848315EDR_F0000_0829M4. Illumination from lower right. (c) Close up view of the inside of the mole pit showing steep walls and several resistant layers with overhangs (arrow). Image D000M0235_617390563EDR_F0000_0817M7. Illumination from overhead.

dust overlying a few cm of unconsolidated sand, which is underlain by a cemented duricrust of variable cm thickness. At *Homestead* hollow, possible clods are seen in a few places directly adjacent to the lander (Figure 12a). Circular cross imprints of the underside of the HP3 feet and the very smooth and reflective imprint of the flat base of the lander scoop on the surface (Figure 12b) suggest the soils have some cohesion (1–1.9 kPa; Golombek et al., 2020) and compress when pressure is exerted, likely due to the presence of finer, unresolved particles. The HP3 mole was initially able to penetrate down to ~35 cm in the hollow soil before stopping. An ~5 cm wide and deep open pit is now observed around the mole. The walls of this pit are near vertical, and there are resistant layers with overhangs (Figure 12c). The strong layers at depth in the mole pit and the steep pits produced beneath the lander during descent are best explained by cementation in an indurated regolith or duricrust (Ansan et al., 2019; Golombek et al., 2020).

7.2. Laguna Hollow Soils

At *Laguna* hollow, sharp edges and slopes of up to 65° (Arvidson et al., 2004) are observed along the 6–7 cm deep trench wall, and an overhanging ledge is seen at the top of the trench (Figure 10c). These observations indicate that some form of cohesion in the upper few centimeters of soil is necessary to produce these features in the trench wall. Arvidson et al. (2004) calculated cohesion values of ~1 kPa that they attributed to electrostatic forces or a modest degree of cementation. Additional calculations of cohesion using telemetry analysis of motor currents during trenching activities on Spirit yielded a value of 0.7 ± 0.7 kPa for the first wheel dig into the *Laguna* hollow regolith (Sullivan et al., 2011). Rover images show the upper soils consists of sandy materials dominated by grains ~100 μ m and smaller sizes and increasing fractions of mixed-in reddish dust at greater excavation depths (Sullivan et al., 2011). Measurements of composition derived from the Mossbauer and Alpha Particle X-Ray Spectrometer (APXS) instruments on Spirit indicate the soils exposed within the *Laguna* trench are basaltic in composition with a similar mineralogy to weakly to moderately altered basaltic rocks (Gellert et al., 2006; Morris et al., 2006). The soils exposed within the *Laguna* trench have an enrichment of Cr and Br relative to the surface soils outside the trench, which could indicate the presence of salts in the subsurface (Gellert et al., 2006; Yen et al., 2005).

Compacted soil clods with sharp edges are seen along the *Laguna* trench floor where the rover wheels pressed down on the soils. Other clods that were produced on the bottom of the trench by wheel compaction were subsequently excavated from the trench and deposited intact in a pile of dug up soil (Figure 10d). If the soil were made of fine dust and sands that lacked cohesion, then these clods should have fallen apart as they were pushed outside of the trench by the rover wheels. Instead, the clods retained their shape, suggesting some process is maintaining cohesion in the soils.

8. Discussion

Our results at both the InSight and Spirit landing sites reveal many similarities in morphology and physical properties of hollows, with the Spirit hollows providing insight into what the pristine prelanding *Homestead*

hollow may have looked like. The main difference between hollows at the two sites is evident in HiRISE orbital images, which show the Spirit hollows have soils that are brighter and redder relative to the surrounding intercrater plains, whereas InSight hollows have soils that generally look similar to the adjacent plains. This difference in soil appearance between the two sites is most likely a result of the greater abundance of darker eolian sands and (or) lower abundance of dust at the Spirit site relative to the InSight landing site. Orbital images taken of Gusev crater outside of this zone with dark sands where Spirit landed show the soils in the intercrater plains and within craters/hollows appear similar, which is more analogous to the InSight landing site. Surface images of hollows taken by the Spirit rover show small eolian ripples are typically present, whereas they are not found in *Homestead* hollow, perhaps because they were removed by the retrorockets during landing or due to the paucity of eolian bedforms at the InSight landing site relative to Gusev crater as seen in orbital images.

Both *Laguna* and *Homestead* hollows have very similar clast sizes, with most resolvable clasts between 3 and 7 mm in length at both sites, although images of other hollows taken by the Spirit rover show some hollows have larger clasts that dominate the hollow interior where the eolian dust mantle is thinner (e.g., *Sleepy* hollow). Nevertheless, the upper hollow surface at both sites is dominated by granules and pebbles compared to the larger rock populations observed in the intercrater plains. These results are consistent with the development of hollows by degradation of the crater rim and infilling of the crater by preferential preservation/accumulation of fines within a topographic depression (Golombek, Crumpler, et al., 2006; Grant et al., 2020; Grant, Arvidson, et al., 2006; Sweeney et al., 2018; Warner et al., 2020). The clast sizes and shapes are consistent with the development of basaltic clasts by impact fragmentation at both sites (Charalambous et al., 2019; Grant, Wilson, et al., 2006) in volcanic plains that date to the Amazonian to Hesperian (Golombek, Crumpler, et al., 2006; Milam et al., 2003; Warner et al., 2017; Wilson et al., 2020). For comparison, Yingst et al. (2008) measured 935 clasts imaged along the traverse of the Spirit rover from Sols 450 to 745 in the Columbia Hills and found most clasts were between 7 and 12 mm in size with a mean value of 11 mm. Clasts were even larger at the Mars Pathfinder site, with sizes ranging from 10 to 950 mm and a mean size of 110 mm (Yingst et al., 2007). The smaller sizes we measured in *Homestead* and *Laguna* hollows are in agreement with the enhanced accumulation of smaller clasts, sand, and dust within these depressions over time relative to other terrains.

Orbital data were used by Golombek et al. (2017) to calculate a thermal inertia of $\sim 200 \text{ Jm}^{-2}\text{K}^{-1}\text{s}^{-1/2}$ for the InSight landing region, which correlates to an upper surface composed of unconsolidated sand size particles, some rocks, and thermally thin coatings of dust. The RAD instrument on InSight also confirmed this thermal inertia after landing (Golombek et al., 2020). The lander camera images and our measurements provide additional ground truth that confirms an upper surface dominated by sand grains (below the resolution of the IDC but inferred from disturbed soils), granules, and pebbles, with a few larger cobbles and boulders interspersed in the regolith.

Both *Homestead* and *Laguna* hollow show evidence for cohesion in the soils. Images at both hollows show imprints and flattening of the soils by the instruments and rover wheels, which could be due to compression of fine, dust-size particles. However, images of the ~ 5 cm deep pit produced by the HP3 mole show near vertical edges and overhangs that are consistent with some form of induration/cementation. Images taken of the *Laguna* hollow trench by Spirit also indicate that induration/cementation is needed to explain the high slopes along the trench walls, overhanging soil layers exposed in the trench, and excavated clods of soils. Cohesion in the Martian soils could be due to cementation, chemical bonding, electrostatic attraction, or other processes in the regolith (Sullivan et al., 2011). An indurated regolith or duricrust has been proposed to explain the cohesion in the upper soils at several other landing sites on Mars (Golombek et al., 2020; Jakosky & Christensen, 1986). One possible process for duricrust formation is when thin films of liquid water precipitated from atmospheric water vapor interact with soils and mobilize soluble species to produce cementation upon evaporation, as suggested by chemical measurements made by Viking and MER (Arvidson et al., 2004; Banin et al., 1992; Haskin et al., 2005; Hurowitz et al., 2006). In particular, the enrichment of Br in the trench soils at *Laguna* hollow can be explained by liquid water mobilizing the ions in salts under current climatic conditions by frost deposition and sublimation over geologic timescales (Yen et al., 2005), and this may be a plausible process that allowed development of a duricrust at both *Laguna* and *Homestead* hollows in volcanic terrains that lack evidence for aqueous activity at the surface.

Our results are consistent with the formation and modification of small (up to tens of meters in diameter), bowl-shaped, pristine impact structures at the InSight and Spirit landing sites that ultimately resulted in features resembling *Homestead* and Spirit hollows. The formation of small craters visible at both sites excavated basaltic, impact-generated regolith (Golombek et al., 2020; Warner et al., 2020), and deposited a surrounding ejecta deposit, consisting of coarse and mostly fine fragments, that was in disequilibrium with local geomorphic thresholds (Golombek, Grant, et al., 2006; Golombek et al., 2020; Grant et al., 2004, 2020; Grant, Arvidson, et al., 2006; Warner et al., 2020). Craters initially experienced relatively rapid degradation by mostly eolian and lesser impact processes and mass-wasting processes (Grant et al., 2004, 2020; Warner et al., 2020) that stripped fines from their rims and deposited them downwind where they became concentrated in their interiors, confirmed by our clast size measurements. Early degradation (e.g., the first ~0.1 Ga at *Homestead* hollow; Grant et al., 2020; Warner et al., 2020) continued until surfaces were stabilized by lags and the inventory of fines was depleted. Subsequent, longer-term degradation for most of a crater's history (e.g., ~0.3–0.6 Ga at *Homestead* hollow; Grant et al., 2020; Warner et al., 2020) in both locations occurred much more slowly and was punctuated by small nearby impacts that emplaced some rocks as ejecta and created small inventories of fine sediments for limited additional eolian infilling. Even lesser sediments were derived from the very slow production of fines via weathering of resistant basaltic rocks (Golombek, Grant, et al., 2006; Golombek et al., 2020; Grant et al., 2004, 2020; Warner et al., 2020). The estimated, time-averaged (order of 0.1 to 1 Ga) erosion rate of 10 to 100-m-scale craters at the InSight landing site is 10^{-4} m Myr⁻¹, which is similar (within an order of magnitude) to other Hesperian to Amazonian-age landscapes and consistent with relatively slow surface processes (e.g., impacts, wind, and mass wasting) that are similar to those observed on modern Mars (Golombek, Grant, et al., 2006; Golombek et al., 2014; Sweeney et al., 2018; Warner et al., 2020).

9. Conclusions

Hollows at both the InSight and Spirit landing sites are similar in appearance with degraded rims and soils infilling the crater interiors. *Sleepy* hollow at the Spirit landing site has eolian ripples and dust on the hollow floor, with some small patches of densely clustered rocks observed where the soil cover is thinner. *Laguna* hollow in Gusev crater exhibits a smooth, bright floor and a degraded rim. There are numerous pebbles and cobbles on the *Laguna* hollow floor that increase in abundance moving radially away from the interior and toward the rim. Eolian ripples of variable height and length occur within the *Laguna* hollow interior, but they are absent from *Homestead* hollow, perhaps due to the retrorockets destroying them during landing. Resolvable clasts (>2 mm) measured at both *Homestead* and *Laguna* hollow have comparable lengths with the majority of the clasts falling between 3 and 7 mm in length and the dominant resolvable particle size between 3 and 4 mm. Measurements of clast shapes show that those in *Laguna* hollow are slightly more elongate relative to those in *Homestead* hollow, although this may be an artifact of the thicker dust mantle obscuring the full shape of clasts at *Laguna* hollow or the different viewing geometries between camera images at both sites.

The upper soils beneath the layer of unconsolidated sand and dust at both hollows show evidence for cohesion, with a trench dug at *Laguna* hollow and pits exposed at *Homestead* hollow exhibiting steep slopes, overhanging layers, and clods of soils. The soil cohesion may have resulted from cementation, chemical bonding, electrostatic attraction, or other processes in the regolith. The similarities in morphology and physical properties of hollows at two different landing sites suggest recent environmental conditions that degrade and infill impact craters are comparable and pervasive across volcanic plains on or near the equatorial regions of Mars.

Data Availability Statement

All data from NASA spacecraft are available in the NASA Planetary Data System archive. All InSight data discussed in this paper are available from the Geosciences node at <https://pds-geosciences.wustl.edu/missions/insight/index.htm>. All HiRISE, CTX, MOLA, MER, and THEMIS data are available from the Cartography and Imaging Node at <https://pds-imaging.jpl.nasa.gov/>. Pancam mosaics are available at the following website: <http://pancam.sese.asu.edu/mosaics.html>. Individual Spirit images can be found at

<https://mars.nasa.gov/mer/gallery/all/spirit.html>. The data used are listed in the figures and (or) repository at the following website: https://figshare.com/authors/Catherine_Weitz/8610882.

Acknowledgments

We thank K. Herkenhoff and R. A. Yingst for providing very helpful comments that greatly improved the quality of this manuscript. A portion of the work was supported by the InSight Project at the Jet Propulsion Laboratory, California Institute of Technology, under Grant 80NSSC18K1625 to J. A. G. C. M. W., and S. A. W. from the National Aeronautics and Space Administration. We are grateful to the InSight science and engineering teams for their efforts to acquire all the data used in this research. We also thank the MRO team for access to the HiRISE and CTX images. Finally, we thank the MER mission for the Spirit images used in this work. The help of Claudia Szczech and Adeli Solmaz in counting clasts in the InSight work space is greatly appreciated. This paper is InSight Contribution Number, ICN-158.

References

- Ansan, V., Hauber, E., Golombek, M., Warner, N., Grant, J., Maki, J., et al. (2019). InSight landing site: Stratigraphy of the regolith beneath the lander and in its surroundings, and implications for formation processes. In *50th Lunar and planetary science, Abstract #1310*. Houston, TX: Lunar and Planetary Science Institute. <https://www.hou.usra.edu/meetings/lpsc2019/pdf/1310.pdf>
- Arvidson, R. E., Anderson, R. C., Bartlett, P., Bell JF 3rd, Blaney, D., Christensen, P. R., et al. (2004). Localization and physical properties experiments conducted by Spirit at Gusev Crater. *Science*, *305*(5685), 821–824. <https://doi.org/10.1126/science.1099922>
- Banin, A., Clark, B. C., & Wänke, H. (1992). Surface chemistry and mineralogy. In H. H. Kieffer, B. M. Jakosky, C. W. Snyder, & M. S. Matthews (Eds.), *Mars* (pp. 594–625). Press, Tucson: University of Arizona.
- Bell, J. F. (2004). Pancam multispectral imaging results from the Spirit Rover at Gusev Crater. *Science*, *305*, (5685), 800–806. <https://doi.org/10.1126/science.1100175>
- Bell, J. F. III, Squyres, S. W., Herkenhoff, K. E., Maki, J. N., Arneson, H. M., Brown, D., et al. (2003). Mars Exploration Rover Athena Panoramic Camera (Pancam) investigation. *Journal of Geophysical Research*, *108*(E12), 8063. <https://doi.org/10.1029/2003JE002070>
- Cabrol, N. A., Grin, E. A., Carr, M. H., Sutter, B., Moore, J. M., Farmer, J. D., et al. (2003). Exploring Gusev Crater with MER A: Review of science objectives and testable hypotheses. *Journal of Geophysical Research*, *108*(E12), 8076. <https://doi.org/10.1029/2002JE002026>
- Charalambous, C., Golombek, M., Pike, T., Warner, N. H., Weitz, C., Ansan, V., et al. (2019). Rock distributions at the InSight landing site and implications based on fragmentation theory. In *50th Lunar and planetary science, Abstract #2812*. Houston, TX: Lunar and Planetary Science Institute. <https://www.hou.usra.edu/meetings/lpsc2019/pdf/2812.pdf>
- Craddock, R. A., & Golombek, M. P. (2016). Characteristics of terrestrial basaltic rock populations: Implications for Mars lander and rover science and safety. *Icarus*, *274*, 50–72. <https://doi.org/10.1016/j.icarus.2016.02.042>
- Crisp, J. A., Adler, M., Matijevic, J. R., Squyres, S. W., Arvidson, R. E., & Kass, D. M. (2003). Mars exploration rover mission. *Journal of Geophysical Research*, *108*(E12), 8061. <https://doi.org/10.1029/2002JE002038>
- Folk, R. L. (1974). *Petrology of sedimentary rocks*. Austin, TX: Hemphill.
- Garvin, J. B., Mouginis-Mark, P. J., & Head, J. W. (1981). Characterization of rock populations on planetary surfaces: Techniques and a preliminary analysis of Mars and Venus. *Moon and the Planets*, *24*(3), 355–387. <https://doi.org/10.1007/BF00897109>
- Geissler, P. E., Sullivan, R., Golombek, M., Johnson, J. R., Herkenhoff, K., Bridges, N., et al. (2010). Gone with the wind: Eolian erasure of the Mars Rover tracks. *Journal of Geophysical Research*, *115*, E00F11. <https://doi.org/10.1029/2010JE003674>
- Gellert, R., Rieder, R., Brückner, J., Clark, B. C., Dreibus, G., Klingelhöfer, G., et al. (2006). Alpha Particle X-Ray Spectrometer (APXS): Results from Gusev crater and calibration report. *Journal of Geophysical Research*, *111*, E02S05. <https://doi.org/10.1029/2005JE002555>
- Golombek, M. P., Crumpler, L. S., Grant, J. A., Greeley, R., Cabrol, N. A., Parker, T. J., et al. (2006). Geology of the Gusev cratered plains from the Spirit rover traverse. *Journal of Geophysical Research*, *111*, E02S07. <https://doi.org/10.1029/2005JE002503>
- Golombek, M. P., Grant, J. A., Crumpler, L. S., Greeley, R., Arvidson, R. E., Bell, J. F. III, et al. (2006). Erosion rates at the Mars Exploration Rover landing sites and long-term climate change on Mars. *Journal of Geophysical Research*, *111*, E12S10. <https://doi.org/10.1029/2006JE002754>
- Golombek, M. P., Warner, N. H., Ganti, V., Lamb, M. P., Parker, T. J., Ferguson, R. L., & Sullivan, R. (2014). Small crater modification on Meridiani Planum and implications for erosion rates and climate change on Mars. *Journal of Geophysical Research: Planets*, *119*, 2522–2547. <https://doi.org/10.1002/2014JE004658>
- Golombek, M., Warner, N. H., Grant, J. A., Hauber, E., Ansan, V., Weitz, C. M., et al. (2020). Geology of the InSight landing site on Mars. *Nat Commun*, *11*, 1014. <https://doi.org/10.1038/s41467-020-14679-1>
- Golombek, M. P., Grant, J. A., Parker, T. J., Kass, D. M., Crisp, J. A., Squyres, S. W., et al. (2003). Selection of the Mars Exploration Rover landing sites. *Journal of Geophysical Research*, *108*(E12), 8072. <https://doi.org/10.1029/2003JE002074>
- Golombek, M. P., Grott, M., Kargl, G., Andrade, J., Marshall, J., Warner, N., et al. (2018). Geology and physical properties investigations by the InSight Lander. *Space Science Reviews*, *214*(5), 84. <https://doi.org/10.1007/s11214-018-0512-7>
- Golombek, M., Kipp, D., Warner, N., Daubar, I. J., Ferguson, R., Kirk, R. L., et al. (2017). Selection of the InSight Landing Site. *Space Sci Rev*, *211*, 5–95. <https://doi.org/10.1007/s11214-016-0321-9>
- Grant, J. A., Arvidson, R. E., Bell, J. F. III, Cabrol, N. A., Carr, M. H., Christensen, P. R., et al. (2004). Surficial deposits at Gusev crater along Spirit rover traverses. *Science*, *305*(5685), 807–810. <https://doi.org/10.1126/science.1099849>
- Grant, J. A., Arvidson, R. E., Crumpler, L. S., Golombek, M. P., Hahn, B., Haldemann, A. F. C., et al. (2006). Crater gradation in Gusev Crater and Meridiani Planum, Mars. *Journal of Geophysical Research*, *111*, E02S08. <https://doi.org/10.1029/2005JE002465>
- Grant, J. A., Warner, N. H., Weitz, C. M., Golombek, M. P., Wilson, S. A., Baker, M., et al. (2020). Degradation of Homestead hollow at the InSight landing site based on the distribution and properties of local deposits. *Journal of Geophysical Research*, *125*, e2019JE006350. <https://doi.org/10.1029/2019JE006350>
- Grant, J. A., Wilson, S. A., Ruff, S. W., Golombek, M. P., & Koestler, D. L. (2006). Distribution of rocks on the Gusev Plains and on Husband Hill, Mars. *Geophysical Research Letters*, *33*, L16202. <https://doi.org/10.1029/2006GL026964>
- Greeley, R., Foing, B. H., McSween, H. Y. Jr., Neukum, G., Pinet, P., van Kan, M., et al. (2005). Fluid lava flows in Gusev crater, Mars. *Journal of Geophysical Research*, *110*, E05008. <https://doi.org/10.1029/2005JE002401>
- Haskin, L. A., Wang, A., Jolliffe, B. L., McSween, H. Y., Clark, B. C., Des Marais, D. J., et al. (2005). Water alteration of rocks and soils on Mars at the Spirit rover site in Gusev crater. *Nature*, *436*(7047), 66–69. <https://doi.org/10.1038/nature03640>
- Herkenhoff, K. E., Squyres, S. W., Anderson, R., Archinal, B. A., Arvidson, R. E., Barrett, J. M., et al. (2006). Overview of the Microscopic Imager Investigation during Spirit's first 450 sols in Gusev crater. *Journal of Geophysical Research*, *111*, E02S04. <https://doi.org/10.1029/2005JE002574>
- Hurowitz, J. A., McLennan, S. M., Tosca, N. J., Ming, D. W., & Schroder, C. (2006). In situ and experimental evidence for acidic weathering of rocks and soils on Mars. *Journal of Geophysical Research*, *111*, E02S19. <https://doi.org/10.1029/2005JE002515>
- Jakosky, B. M., & Christensen, P. R. (1986). Global duricrust on Mars: Analysis of remote-sensing data. *Journal of Geophysical Research*, *91*(B3), 3547–3559. <https://doi.org/10.1029/JB091iB03p03547>
- Krumbein, W. C., & Sloss, L. L. (1951). *Stratigraphy and sedimentation* (Vol. 71, pp. 5–401). San Francisco: W. H. Freeman.
- Lognonné, P., Banerdt, W. B., Giardini, D., Pike, W. T., Christensen, U., Laudet, P., et al. (2019). SEIS: Insight's Seismic Experiment for Internal Structure of Mars. *Space Science Reviews*, *215*, 12. <https://doi.org/10.1007/s11214-018-0574-6>

- Lognonné, P., Banerdt, W. B., Pike, W. T., Giardini, D., Christensen, U., Garcia, R. F., et al. (2020). Constraints on the shallow elastic and anelastic structure of Mars from InSight seismic data. *Nature Geoscience*, 13(3), 213–220. <https://doi.org/10.1038/s41561-020-0536-y>
- Maki, J. N., Bell, J. F. III, Herkenhoff, K. E., Squyres, S. W., Kiely, A., Klimesh, M., et al. (2003). Mars Exploration Rover engineering cameras. *Journal of Geophysical Research*, 108(E12), 8071. <https://doi.org/10.1029/2003JE002077>
- Maki, J. N., Golombek, M., Deen, R., Abarca, H., Soric, C., Goodsall, T., et al. (2018). The color cameras on the InSight lander. *Space Science Reviews*, 214, 105. <https://doi.org/10.1007/s11214-018-0536-z>
- Malin, M. C., Bell, J. F. III, Cantor, B. A., Caplinger, M. A., Calvin, W. M., Clancy, R. T., et al. (2007). Context Camera Investigation on board the Mars Reconnaissance Orbiter. *Journal of Geophysical Research*, 112, E05S04. <https://doi.org/10.1029/2006JE002808>
- McEwen, A. S., Eliason, E. M., Bergstrom, J. W., Bridges, N. T., Hansen, C. J., Delamere, W. A., et al. (2007). Mars Reconnaissance Orbiter's High Resolution Imaging Science Experiment (HiRISE). *Journal of Geophysical Research: Planets*, 112, E05S02. <https://doi.org/10.1029/2005JE002605>
- Milam, K. A., Stockstill, K. R., Moersch, J. E., McSween, H. Y. Jr., Tornabene, L. L., Ghosh, A., et al. (2003). THEMIS characterization of the MER Gusev crater landing site. *Journal of Geophysical Research*, 108(E12), 8078. <https://doi.org/10.1029/2002JE002023>
- Morris, R. V., Klingelhöfer, G., Schröder, C., Rodionov, D. S., Yen, A., Ming, D. W., et al. (2006). Mossbauer mineralogy of rock, soil, and dust at Gusev crater, Mars: Spirit's journey through weakly altered olivine basalt on the plains and pervasively altered basalt in the Columbia Hills. *Journal of Geophysical Research*, 111, E02S13. <https://doi.org/10.1029/2005JE002584>
- Powers, M. C. (1953). A new roundness scale for sedimentary particles. *Journal of Sedimentary Petrology*, 23, 17–19. <https://doi.org/10.1306/d4269567-2b26-11d7-8648000102c1865d>
- Richter, L., Schmitz, N., Weiss, S., & MER/Athena Team (2006). Inferences of strength of soil deposits along MER Rover traverses. In *paper presented at 1st European Planetary Science Congress*. Berlin: Eur. Planetol. Network.
- Schneider, C. A., Rasband, W. S., & Eliceiri, K. W. (2012). NIH image to ImageJ: 25 years of image analysis. *Nature Methods*, 9, 671–675. <https://doi.org/10.1038/nmeth.2089>
- Smith, D. E., Zuber, M. T., Frey, H. V., Garvin, J. B., Head, J. W., Muhleman, D. O., et al. (2001). Mars Orbiter Laser Altimeter: Experiment summary after the first year of global mapping of Mars. *Journal of Geophysical Research*, 106(E10), 23,689–23,722. <https://doi.org/10.1029/2000JE001364>
- Spohn, T., Grott, M., Smrekar, S. E., Knollenberg, J., Hudson, T. L., Krause, C., et al. (2018). The heat flow and physical properties package (HP3) for the InSight mission. *Space Science Reviews*, 214(5), 96. <https://doi.org/10.1007/s11214-018-0531-4>
- Squyres, S. W., Arvidson, R. E., Bell JF 3rd, Brückner, J., Cabrol, N. A., Calvin, W., et al. (2004). The Spirit Rover's Athena science investigation at Gusev Crater Mars. *Science*, 305(5685), 794–799. <https://doi.org/10.1126/science.3050794>
- Sullivan, R., Anderson, R., Biesiadecki, J., Bond, T., & Stewart, H. (2007). Martian regolith cohesions and angles of internal friction from analysis of MER wheel trenches. *Lunar and Planetary Science, XXXVIII*. abstract 2084. <https://www.lpi.usra.edu/meetings/lpsc2007/pdf/2084.pdf>
- Sullivan, R., Anderson, R., Biesiadecki, J., Bond, T., & Stewart, H. (2011). Cohesions, friction angles, and other physical properties of Martian regolith from Mars Exploration Rover wheel trenches and wheel scuffs. *Journal of Geophysical Research*, 116, E02006. <https://doi.org/10.1029/2010JE003625>
- Sweeney, J., Warner, N. H., Ganti, V., Golombek, M. P., Lamb, M. P., Fergason, R., & Kirk, R. (2018). Degradation of 100-m-scale impact craters at the InSight landing site on Mars with implications for surface processes and erosion rates in the Hesperian and Amazonian. *Journal of Geophysical Research*, 123, 2732–2759. <https://doi.org/10.1029/2018JE005618>
- Tanaka, K. L., Skinner, J. A. Jr., Dohm, J. M., Irwin, R. P. III, Kolb, E. J., Fortezzo, C. M., et al. (2014). Geologic map of Mars. *U.S. Geological Survey Scientific Investigations Map*, 3292. <https://doi.org/10.3133/sim3292>
- Trebi-Ollennu, A., Kim, W., Ali, K., et al. (2018). InSight Mars lander robotics instrument deployment system. *Space Science Reviews*, 214, 93. <https://doi.org/10.1007/s11214-018-0520-7>
- Wadell, H. (1932). Volume, shape, and roundness of rock particles. *Journal of Geology*, 40(5), 443–451. <https://doi.org/10.1086/623964>
- Warner, N. H., Golombek, M. P., Sweeney, J., Fergason, R., Kirk, R., & Schwartz, C. (2017). Near surface stratigraphy and regolith production in southwestern Elysium Planitia, Mars: Implications for Hesperian–Amazonian terrains and the InSight lander mission. *Space Science Reviews*, 211(1–4), 147–190. <https://doi.org/10.1007/s11214-017-0352-x>
- Warner, N. H., Grant, J. A., Wilson, S. A., Golombek, M. P., DeMott, A., Charalambous, C., et al. (2020). An impact crater origin for the InSight landing site at Homestead hollow: Implications for near surface stratigraphy, surface processes, and erosion rates. *Journal of Geophysical Research*, 125, e2019JE006333. <https://doi.org/10.1029/2019JE006333>
- Weitz, C. M., Grant, J. A., Warner, N. H., Golombek, M. P., Wilson, S. A., Hauber, E., et al. (2019). Clast sizes and shapes at the InSight landing site. In *50th Lunar and planetary science*, Houston, TX: Lunar and Planetary Science Institute. Abstract #1392. <https://www.hou.usra.edu/meetings/lpsc2019/pdf/1392.pdf>
- Wentworth, C. K. (1922). A scale of grade and class terms for clastic sediments. *Journal of Geology*, 30(5), 1922. <https://doi.org/10.1086/622910>
- Williams, N. R., Golombek, M. P., Warner, N. H., Daubar, I., Hausmann, R., Hauber, E., et al. (2019). Surface alteration from landing InSight on Mars and its implications for shallow regolith structure. In *50th Lunar and planetary science*, Houston, TX: Lunar and Planetary Science Institute. Abstract #2781. <https://www.hou.usra.edu/meetings/lpsc2019/pdf/2781.pdf>
- Wilson, S. A., Warner, N. H., Grant, J. A., Golombek, M. P., & Weitz, C. M. (2020). Comparison of crater retention ages at the InSight and Spirit landing sites. In *51st Lunar and planetary science*. Houston, TX: Lunar and Planetary Science Institute. Abstract #2247. <https://www.hou.usra.edu/meetings/lpsc2020/pdf/2247.pdf>
- Yen, A. S., Gellert, R., Schröder, C., Morris, R. V., Bell, J. F. III, Knudson, A. T., et al. (2005). An integrated view of the chemistry and mineralogy of Martian soils. *Nature*, 436(7047), 49–54. <https://doi.org/10.1038/nature03637>
- Yingst, R. A., Crumpler, L., Farrand, W. H., Li, R., Cabrol, N. A., & Neakrase, L. D. (2008). Morphology and texture of particles along the Spirit rover traverse from sol 450 to sol 745. *Journal of Geophysical Research*, 113, E12S41. <https://doi.org/10.1029/2008JE003179>
- Yingst, R. A., Haldemann, A. F. C., Biedermann, K. L., & Monhead, A. M. (2007). Quantitative morphology of rocks at the Mars Pathfinder landing site. *Journal of Geophysical Research*, 112, E06002. <https://doi.org/10.1029/2005JE002582>
- Yingst, R. A., Kah, L. C., Palucis, M., Williams, R. M. E., Garvin, J., Bridges, J. C., et al. (2013). Characteristics of pebble- and cobble-sized clasts along the Curiosity rover traverse from Bradbury Landing to Rocknest. *Journal of Geophysical Research: Planets*, 118, 2361–2380. <https://doi.org/10.1002/2013JE004435>